Spin Electronics

Correlation Between Disordered Magnetic Phases in Ferromagnetic/Antiferromagnetic Thin Films and Device-to-Device Variability of Exchange Bias in Spintronic Applications

Kamil Akmaldinov[1,2,3,4], Lamprini Frangou[1,2,3], Clarisse Ducruet[4], Céline Portemont[4], Jérémy Pereira[4], Isabelle Joumard[1,2,3], Bernard Dieny[1,2,3*], Jérémy Alvarez-Hérault[4], and Vincent Baltz[1,2,3]

[1] *Univ. Grenoble Alpes, SPINTEC, F-38000 Grenoble, France*
[2] *CNRS, SPINTEC, F-38000 Grenoble, France*
[3] *CEA, INAC-SPINTEC, F-38000 Grenoble, France*
[4] *CROCUS Technology, F-38000 Grenoble, France*
[*] *Senior Member, IEEE*

Received 1 Jun 2015, revised 22 Jun 2015, accepted 27 Jun 2015, published 6 Jul 2015, current version 7 Aug 2015.

Abstract—Spintronic applications rely on ferromagnetic/antiferromagnetic exchange biased bilayers. In this study, we show whether and how disordered magnetic phases, which exhibit low freezing temperatures and are located in the ferromagnetic/antiferromagnetic thin film, affect the device-to-device variability of exchange bias in magnetic applications once the film is nanofabricated.

Index Terms—Spin electronics, disordered magnetic phases, exchange bias, device variability, magnetic random-access memory, blocking temperature distribution.

I. INTRODUCTION

Exchange bias (EB) [Nogués 1999], which results from the magnetic exchange interactions between ferromagnetic (F) and antiferromagnetic (AF) materials, is used in a large variety of spintronic devices. Besides the influence of the F and AF bulk properties, the EB effects depend strongly on the interfacial uncompensated AF spins that magnetically couple the F and the AF materials [Ohldag 2003]. For a given F/AF bilayer, the uncompensated AF spins can be split into two groups depending on the AF entity to which they belong: stable grains [Fulcomer 1972] or disordered magnetic phases [Takano 1997]. Essentially, theory and simulations propose that some of the microscopic mechanisms accounting for the EB manifestations are comparable to the behavior of disordered or spin-glass-like phases that exhibit low freezing temperatures [Berkowitz 1999, Lhoutellier 2015]. Different terminologies now describe the same idea: low freezing temperature spins [Takano 1997], spin-glass-like regions/phases [Baltz 2010b]; spin clusters [O'Grady 2010], and disordered magnetic phases [Lhoutellier 2015]. Here, we will stick to the terminology "disordered magnetic phases" since the impact of such phases will be discussed for temperatures ranging above their ordering temperatures. Experimentally, the amount of disordered magnetic phases is accessible by several techniques, including blocking temperature distributions [Soeya 1994, Baltz 2010b]. In the literature, the quantitative impact of various parameters was considered, such as the F/AF interfacial mixing, the AF crystallography, lateral sizes, and the nature of the AF material. In particular, the amount of Mn-content in Mn-based AF materials strongly influences the quantity of disordered magnetic phases. In fact, by using $Ir_{20}Mn_{80}$ (at.%), $Fe_{50}Mn_{50}$, and $Ir_{20}Mn_{80}/Fe_{50}Mn_{50}$, $Fe_{50}Mn_{50}/Ir_{20}Mn_{80}$ multilayers, it is possible to tune the amount of disordered phases in continuous films [Akmaldinov 2014].

Since disordered magnetic phases are spread over the F/AF films, the question tackled here concerns the impact of such a basic phenomenon on technological applications. Indeed, whether disordered magnetic phases located at the F/AF interface of the continuous film also regulate the device-to-device variability of EB in spintronic applications remains an important, open question. Actually, in the case of magnetic random-access memory (MRAM) applications, the problem of cell-to-cell variability was raised since the very first generation of chips. Most works focused on the variability of the cell shape that arises during the nanofabrication processes [Slaughter 2010]. In this letter, we will deal with the correlation between disordered magnetic phases above F/AF films and cell-to-cell variability of EB in functional thermally-assisted MRAM (TA-MRAM) chips.

II. EXPERIMENTS

The following multilayers are studied: CMOS//buffer/[AF_1/Ru2/F_1]/MgO1.4/[F_2/AF_2]/thermal barrier/cap (nm), with AF_1 = PtMn20; F_1 = CoFeB1.2; F_2 = CoFeB2/NiFe1.5, and AF_2 = IrMn10; $\{IrMn1/FeMn1\}_{\times 5}$, $\{FeMn1/IrMn1\}_{\times 5}$ and FeMn10. CMOS stands for complementary metal-oxide semiconductor. The total thickness of AF_2 is kept constant. The multilayer structures are deposited by dc magnetron sputtering with an Ar pressure of 2.5×10^{-3} mbar onto 8-in standard CMOS wafers with typical preprocessed back-end transistors. In the multilayer structures, PtMn, NiFe, CoFeB, IrMn, and FeMn are made from $Pt_{38}Mn_{62}$, $N_{i81}Fe_{19}$, $Co_{60}Fe_{20}B_{20}$, $Ir_{20}Mn_{80}$, and $Fe_{50}Mn_{50}$ targets (at.%). Here, we specifically worked on the EB properties of the [F_2/AF_2] storage layer. Therefore, to ease the data interpretation and in contrast to the TA-MRAM final product

Corresponding author: V. Baltz (vincent.baltz@cea.fr).
Digital Object Identifier 10.1109/LMAG.2015.2452891

[Prejbeanu 2013], the [AF_1/Ru2/F_1] reference layer is downgraded to a simple free layer by decoupling AF_1 and F_1 with a thick Ru spacer. For similar reasons, we used F layers instead of synthetic-AF stacks. Room-temperature EB is set by postdeposition field-cooling (FC) of the samples for 90 min in a resistive furnace from 300 °C down to room-temperature. The vacuum level during annealing is set to 10^{-6} mbar. Positive magnetic field during cooling is applied in the sample plane, with an amplitude of 10 kOe, large enough to saturate the F_2 layer. The amount of disordered magnetic phases in the continuous film is varied by changing the nature of the AF_2 material.

In order to set the basis for this study, the typical blocking temperature distributions [Soeya 1994] of the thin films are then checked with a vibrating sample magnetometer (VSM) and by use of a standard FC procedure. Essentially, all the AF entities are initially set positively via a positive FC. From this state, negative FC from incremental annealing temperatures gradually resets the AF entities toward the negative direction. Hysteresis loop measurements after each increment records the progressive reorientation of the AF entities. Besides the AF grain volume distribution giving rise to a "high" temperature contribution, a "low" temperature contribution is observed and attributed to the disordered phases [Baltz 2010a, 2010b]. The relative amount of disordered magnetic phases spread over the sheet wafer (Δ^*) is extracted from the relative weight of the high and low temperature contributions. For the samples involved in this paper, for the four multilayer compositions, we obtained, as expected and in agreement with previous findings [Akmaldinov 2014]: $\Delta^* = 52$, 40, 36, and 27%, corresponding to $AF_2 = IrMn10$; $\{IrMn1/FeMn1\}_{\times 5}$, $\{FeMn1/IrMn1\}_{\times 5}$, and FeMn10 (nm), respectively.

Following the verification of the magnetic behavior of the sheet films, the wafers are processed by use of standard cleanroom lithography and etching techniques to obtain two series of TA-MRAM chips with circular magnetic cells of diameter 180 and 240 nm. Fig. 1 is a transmission electron microscopy (TEM) cross section. The image shows two of our magnetic memory cells sandwiched between two metallic contacts: M3 and M4 (dark contrasts) and surrounded by an insulator (bright contrast). The metallic contacts connect the magnetic stack—detailed in the inset—to the bit- and word-lines. Following the process, the electrical properties of individual memory cells of the chips are tested at room temperature by use of an automated electrical prober. A bias voltage of 50 mV is applied between the bit- and word-lines to read the resistance (R) and external coils are used to sweep the magnetic field (H) between $\pm$800 Oe. As a result, for each of the four multilayer compositions, we obtain two sets of around two hundred R versus H loops: one for the 180 nm cells and one for the 240 nm cells.

III. RESULTS AND DISCUSSION

A typical R versus H loop is shown in Fig. 2. The hysteresis loop—magnetization (M) versus field (H)—for the corresponding sheet film measured by VSM at room temperature is also shown in Fig. 2 along with the definition of several magnetic parameters.

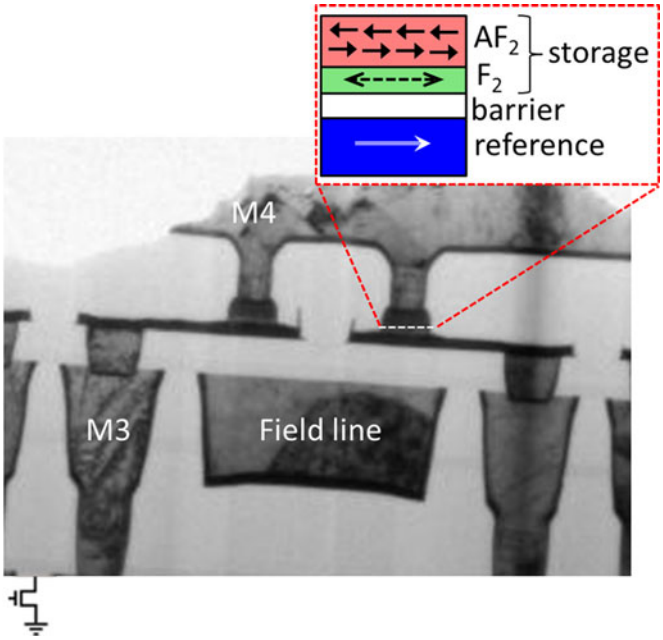

Fig. 1. (a) Transmission electron microscopy (TEM) cross-section enlargement of two memory cells of a typical TA-MRAM chip on CMOS.

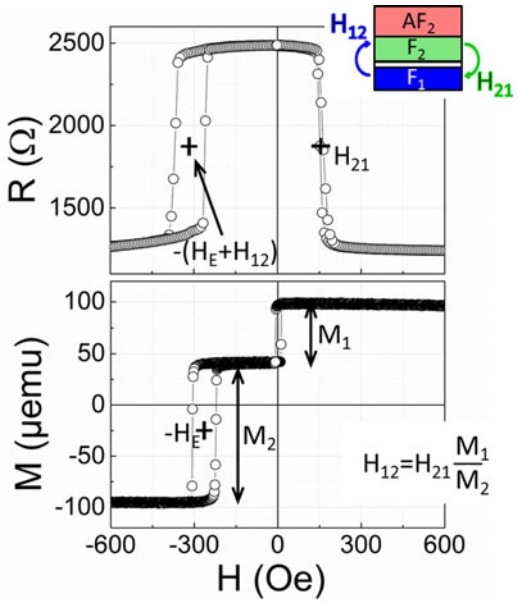

Fig. 2. Top: resistance (R) versus field (H) for a TA-MRAM circular cell with a diameter of 180 nm. The loop shift (H_E) of the F_2/AF_2 storage layer and the stray fields created by F_1 on F_2 (H_{12}) and by F_2 on F_1 (H_{21}) are defined in the graph. Bottom: magnetization *(M)* versus *H* for the corresponding sheet film. H_E is also defined in the graph along with the magnetizations M_1 and M_2 of the F_1 and F_2 layers.

It is reasonable to assume that the layers are conformal in shape. From simple considerations, it thus results that the ratio between stray fields from one layer to another (H_{12}/H_{21}) is equal to the ratio between the layer magnetizations (M_1/M_2). This latter ratio is deduced from the VSM measurement of the sheet film. For every memory cell, it is thus possible to extract the EB loop shift (H_E) from the R versus H data, with $H_E = (H_E + H_{12}) - H_{21} \times (M_1/M_2)$.

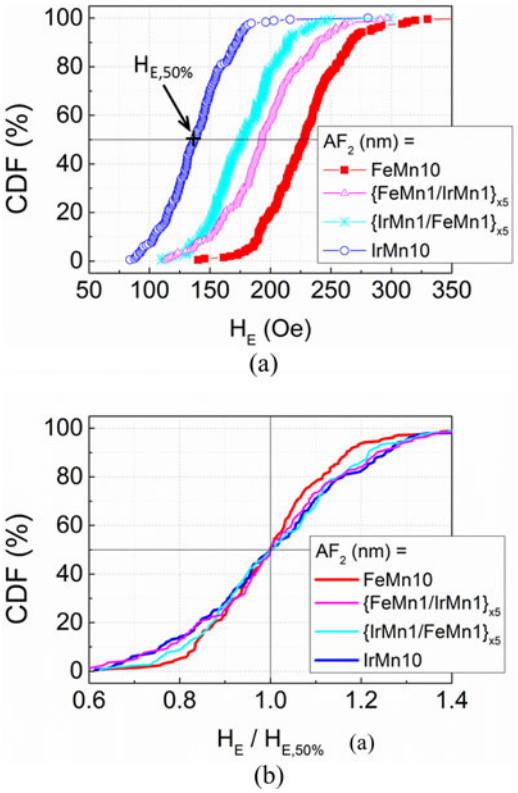

Fig. 3. For TA-MRAM chips, cumulative distribution function of hysteresis loop shift (CDF) over TA-MRAM cells as a function of: (a) the loop shift (H_{E}) and (b) the normalized loop shift ($H_{\mathrm{E}}/H_{\mathrm{E,50\%}}$). Each data point results from the R versus H electrical characterization of an individual TA-MRAM cell. The storage layer compositions are: [$\mathrm{F_2/AF_2}$] with $\mathrm{F_2} = \mathrm{CoFeB2/NiFe1.5}$ (nm) and with $\mathrm{AF_2}$ varied between the four chips. The cell's diameters are 180 nm.

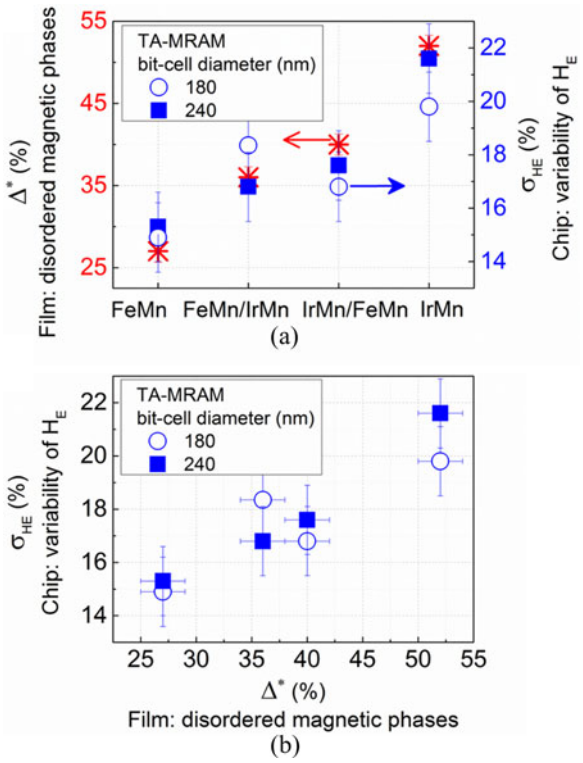

Fig. 4. (a) For four TA-MRAM compositions with various AF materials in the storage layer: $\mathrm{AF_2} = \mathrm{IrMn10}$; $\{\mathrm{IrMn1/FeMn1}\}_{\times 5}$, $\{\mathrm{FeMn1/IrMn1}\}_{\times 5}$ and FeMn10, amount of disordered magnetic phases (Δ^*) in the sheet wafers and cell-to-cell variability of H_{E} (σ_{HE}) over the ~200 cells of the corresponding TA-MRAM chips with cells diameters of 180 and 240 nm. (b) σ_{HE} versus Δ^*.

For the statistical analysis of the cell-to-cell distribution of H_{E} over the TA-MRAM chips, we performed cumulative frequency analysis. It is the analysis of the frequency of occurrence of H_{E}. For the four TA-MRAM chips with four different $\mathrm{AF_2}$ layers, Fig. 3(a) shows the cumulative distribution functions (CDF) versus H_{E}. Note that a data point in the graph corresponds to a measurement of one TA-MRAM cell. The graph reads as follows: for example, when the cumulative distribution equals 30%, the corresponding value of H_{E} is 135 Oe for $\mathrm{AF_2} = \mathrm{IrMn10}$. It means that 30% of the cells have a value of H_{E} that is less than 135 Oe. The value of H_{E} with an occurrence of 50% ($H_{\mathrm{E,50\%}}$) is indicated in Fig. 3(a) for $\mathrm{AF_2} = \mathrm{IrMn10}$. The main point here concerns how the EB loop shift dispersion varies between the different $\mathrm{AF_2}$ layers. To allow comparison of the cumulative distributions for the four compositions, Fig. 3(b) shows the cumulative distributions versus H_{E} normalized to $H_{\mathrm{E,50\%}}$. The standard deviations (σ_{HE}) of these curves account for the cell-to-cell variability of $\mathrm{H_E}$. This latter seems to be larger when the $\mathrm{AF_2}$ layer evolves from pure FeMn to pure IrMn. In order to quantitatively analyze such a cell-to-cell variability of H_{E}, we calculated σ_{HE}.

For the four $\mathrm{AF_2}$ layer compositions, Fig. 4(a) summarizes the amount of disordered magnetic phases (Δ^*) deduced from blocking temperature distributions measurements on the sheet wafers (left axis) and shows σ_{HE} over the TA-MRAM cells of the chips (right axis). The graph recalls that the amount of disordered magnetic phases is varied by means of tuning the $\mathrm{AF_2}$ layer composition. From Fig. 4(a), we see that the two dependences of σ_{HE} with the $\mathrm{AF_2}$ layer composition follow the same trend as that of the amount of disordered magnetic phases; strictly speaking, except for $\mathrm{AF_2} = \mathrm{FeMn/IrMn}$ with 180 nm cells. Actually, the nominally laminated FeMn/IrMn and IrMn/FeMn multilayers most closely resemble FeIrMn alloys in reality [Akmaldinov 2014]. The fact that the values of Δ^* and σ_{HE} are close for $\mathrm{AF_2} = \mathrm{FeMn/IrMn}$ and IrMn/FeMn agrees with that statement. The interplay between the amount of disordered magnetic phases measured at the sheet film level and cell-to-cell variability of H_{E} in TA-MRAM processed chips is better visible in Fig. 4(b), which shows σ_{HE} versus Δ^*. Essentially, the disordered magnetic phases resulting from magnetic frustrations are spread over the wafer and, thus, over the memory cells after nanofabrication as shown in Fig. 5. As opposed to cells with few disordered magnetic phases, cells with more of such phases show a weaker hysteresis loop shift and are more prone to thermal activation since the F/AF interfacial coupling is disrupted on a large part of the cell area.

From the linear relationship possibly assumed from Fig. 4(b), we note that σ_{HE} tends toward about 8% when Δ^* tends to 0. This may give an estimate for the part of the cell-to-cell variability of H_{E} that is independent on the disordered magnetic phases.

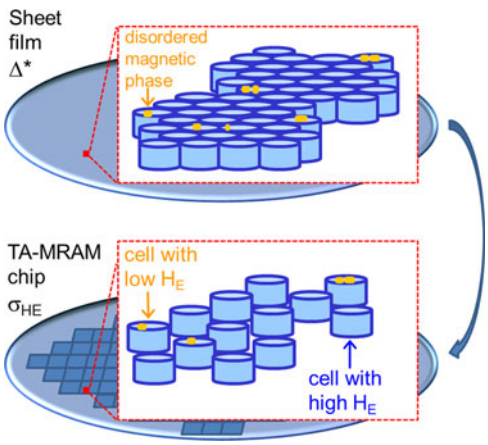

Fig. 5. Sketch showing the spread of disordered magnetic phases (orange dots) over a polycrystalline film and the resulting TA-MRAM cell-to-cell variability of exchange bias after patterning the film in the form of memory cells. To ease the reading, a grain (blue cylinder) defines a cell although in reality each cell contains tens of grains.

This independent part likely originates from process-induced variability in, for example, cell sizes and shapes [Slaughter 2010]. Such types of variability are independent of the sample since all four samples were subject to the same process flow here. Although Fig. 4(b) shows that the amount of disordered magnetic phases influence the variability of H_{E}, finding the exact ratio between these two parameters is not straightforward and trying to push the analysis to a further quantitative level would probably be misleading. In particular, it was shown earlier that patterning adds disordered magnetic phases at the dots' edges: about $+25\%$ for $180\,\mathrm{nm} \times 100\,\mathrm{nm}$ rectangular dots, i.e., $+25\%$ for a perimeter of 560 nm [Baltz 2010a]. It is thus not unlikely that the amount of disordered phases measured for a film underestimates the amount of disordered magnetic phases for the cells, i.e., when one takes into account the film plus the edges. We anticipate that the amount of disordered magnetic phases created by the patterning is proportional to the cell perimeter. This being said, the amount of additional edge disordered magnetic phases is larger for the cells with diameters of 240 nm compared to those with diameters of 180 nm: $+34$ and $+25\%$, respectively, if we roughly consider the previously discussed and measured $+25\%$ for a perimeter of 560 nm. With this scenario, for a given cell size, edge effects would translate the values of Δ^* toward larger values.

IV. CONCLUSION

We demonstrated experimentally the correlation between the amount of disordered magnetic phases spread over F/AF thin films and the device-to-device variability of EB in magnetic applications. The industry mostly uses Mn-based metallic antiferromagnets such as IrMn, FeMn, PtMn, and NiMn. Since Mn-diffusion is a known source of disordered magnetic phases, reducing as much as possible the Mn-content or adding diffusion barriers or getters to avoid Mn-diffusion or finding Mn-free antiferromagnets compatible with industrial constraints are three possible pathways to reduce the subsequent variability of EB properties in devices. This study also highlighted the fact that blocking temperature distribution measurements may turn out to be a complementary useful means for the qualification of magnetic stacks before launching a full nanofabrication process.

REFERENCES

Akmaldinov K, Ducruet C, Portemont C, Joumard I, Prejbeanu I L, Dieny B, Baltz V (2014), "Mixing antiferromagnets to tune NiFe-[IrMn/FeMn] interfacial spin-glasses, grains thermal stability, and related exchange bias properties," *J. Appl. Phys.*, vol. 115, 17B718, doi: 10.1063/1.4864144.

Baltz V, Gaudin G, Somani P, Dieny B (2010a), "Influence of edges on the exchange bias properties of ferromagnetic/antiferromagnetic nanodots," *Appl. Phys. Lett.*, vol. 96, 262505, doi: 10.1063/1.3449123.

Baltz V, Rodmacq B, Zarefy A, Lechevallier L, Dieny B (2010b), "Bimodal distribution of blocking temperature in exchange-biased ferromagnetic/antiferromagnetic bilayers," *Phys. Rev. B*, vol. 81, 052404, doi: 10.1103/PhysRevB.81.052404.

Berkowitz A E, Takano K (1999), "Exchange anisotropy—A review," *J. Magn. Magn. Mater.*, vol. 200, pp. 552–570, doi: 10.1016/S0304-8853(99)00453-9.

Fulcomer E, Charap S H (1972), "Thermal fluctuation aftereffect model for some systems with ferromagnetic-antiferromagnetic coupling," *J. Appl. Phys.*, vol. 43, pp. 4190–4199, doi: 10.1063/1.1660894.

Lhoutellier G, Ledue D, Patte R, Barbe F, Dieny B, Baltz V (2015), "Bimodal distribution of blocking temperature for exchange-bias ferromagnetic/antiferromagnetic bilayers: A granular Monte Carlo study with less stable magnetic regions spread over the interface," *J. Phys. D: Appl. Phys.*, vol. 48, 115001, doi: 10.1088/0022-3727/48/11/115001.

Nogués J, Schuller I K (1999), "Exchange bias," *J. Magn. Magn. Mater.*, vol. 192, pp. 203–232, doi: 10.1016/S0304-8853(98)00266-2.

O'Grady K, Fernandez-Outon L E, Vallejo-Fernandez G (2010), "A new paradigm for exchange bias in polycrystalline thin films," *J. Magn. Magn. Mater.*, vol. 322, pp. 883–899, doi: 10.1016/j.jmmm.2009.12.011.

Ohldag, H, Scholl A, Nolting F, Arenholz E, Maat S, Young A T, Carey M, Stöhr J (2003), "Correlation between exchange bias and pinned interfacial spins," *Phys. Rev. Lett.*, vol. 91, 017203, doi: 10.1103/PhysRevLett.91.017203.

Prejbeanu, I L, Bandiera S, Alvarez-Hérault J, Sousa R C, Dieny B, Nozières J-P (2013), "Thermally assisted MRAMs: Ultimate scalability and logic functionalities," *J. Phys. D: Appl. Phys.*, vol. 46, 074002, doi: 10.1088/0022-3727/46/7/074002.

Slaughter, J M, Rizzo N D, Mancoff F B, Whig R, Smith K, Aggarwal S, Tehrani S (2010), "Toggle and spin-torque MRAM: Status and outlook," *J. Magn. Soc. Jpn.*, vol. 5, pp. 171–176.

Soeya S, Imagawa T, Mitsuoka K, Narishige S (1994), "Distribution of blocking temperature in bilayered $Ni_{81}Fe_{19}$/NiO films," *J. Appl. Phys.*, vol. 76, pp. 5356–5360, doi: 10.1063/1.358488.

Takano K, Kodama R H, Berkowitz A E, Cao W, Thomas G (1997), "Interfacial uncompensated antiferromagnetic spins: Role in unidirectional anisotropy in polycrystalline $Ni_{81}Fe_{19}$/CoO bilayers," *Phys. Rev. Lett.*, vol. 79, pp. 1130–1133, doi: 10.1103/PhysRevLett.79.1130.